Journal of
Materials Chemistry A

Materials for energy and sustainability

Accepted Manuscript

This article can be cited before page numbers have been issued, to do this please use: Y. Li, M. Lu, Y. wu, Q. Ji, H. Xu, J. Gao, G. Qian and Q. Zhang, *J. Mater. Chem. A*, 2020, DOI: 10.1039/D0TA05866A.

ROYAL SOCIETY OF CHEMISTRY

rsc.li/materials-a

View Article Online
DOI: 10.1039/D0TA05866A

ARTICLE

Morphology Regulation of Metal-Organic Framework-Derived Nanostructures for Efficient Oxygen Evolution Electrocatalysis

Yuwen Li[a,c], Mengting Lu[a], Yuhang Wu[a], Qinghong Ji[a], Hui Xu[b], Junkuo Gao,*[a] Guodong Qian,*[c] Qichun Zhang*[d,e]

Received 00th January 20xx,
Accepted 00th January 20xx

DOI: 10.1039/x0xx00000x

Understanding the relationship between the morphology of the same metal-organic framework-derived nanostructures and their performance as the catalysts in oxygen evolution reaction (OER) is very important and highly desirable, because such study would provide a new insight into the systematic regulation of catalysts morphology for performance enhancement in electrocatalysis and photocatalysis. Here, a series of accurate morphology-regulated electrocatalysts (including nanosheets, nanoflowers, nanotubes and aggregations) derived from Hofmann-type metal-organic frameworks (MOFs) are reported for efficient OER. Among all the nanostructures, FeNi nanosheets render the best OER catalytic performance in alkaline media, achieving a low overpotential of 248 mV at 10 mA cm^{-2}, an ultra-small Tafel slope of 31.2 mV dec^{-1} and a satisfactory stability, far more outperforming commercial RuO_2 catalyst. The reason is that FeNi nanosheets possess the optimized conductivity, oxygen vacancies and N-related active sites. Our research also demonstrates that electron transfer can be achieved through the precise control in the morphology of precursor MOFs.

1. Introduction

With the exhaustion of traditional fossil energy and the rapid growth of global environmental pollution, the contradiction between energy demand and environmental protection becomes deeper and deeper.[1–4] Thus, finding a suitable way to solve this issue is urgent and extremely important. Among many novel approaches to the realization of pollution-free energy, electrocatalytic water decomposition under alkaline conditions to produce hydrogen gas has emerged to be a prominent tactic to convert electricity into chemical energy.[5–8] However, the sluggish kinetics and thermodynamics of the multi-step electron transfer OER hinder the process of water splitting.[9–13] Although noble-metal based electrocatalysts (e.g., IrO_2 and RuO_2) have been demonstrated to show excellent catalytic properties, their high cost and low durability largely hamper their commercial applications.[14–17] To address this issue, heteroatom-doped transition metal-based carbonaceous electrocatalysts with high theoretical activity, easy availability, and versatile design have been widely investigated.[18–20] During research, scientists also found that the existence of highly electronegative nitrogen dopants in above-mentioned metal-based carbonaceous electrocatalysts could change the spin distribution of the adjacent C atoms and produce positively charged sites to promote the adsorption and the reduction of oxygen molecules.[21,22] Moreover, the synergistic effects between transition metals and N-doped carbon matrix could change the adsorption ability of the intermediate, thereby boosting the catalytic activities.[23,24]

In addition to the chemical composition, the nanostructure and morphology of electrocatalysts also play a critical role.[25–27] Therefore, the rational design and engineering in the morphology of nanomaterials is necessary, because intricate nanostructures with high specific surface area is essential for the realization of high catalytic activity.[28] Given their several charming advantages such as well-tuneable frameworks, uniform composition and mature porosity, MOFs have received widespread attention as promising sacrificial templates for transition metal-based carbon composites.[29–34] Although a lot of researches have been paid to the regulation of chemical components, systematically studying the fine-tuning of nanostructure is still very limited. In fact, the morphology modulation aiming at increasing the reactivity of the active sites and the mass transfer efficiency is very challenging.[24,35]

Herein, we report a series of FeNi Hofmann type MOF-derived electrocatalysts with different micromorphology, including FeNi nanosheets (FeNi NSs), FeNi nanoflowers (FeNi NFs), FeNi nanotubes (FeNi NTs) and FeNi aggregations (FeNi AGs), by facilely tuning the concentration of MOF precursors with/out the addition of the nontoxic surfactant polyvinyl pyrrolidone (PVP) at room temperature. The accurate

[a] Institute of Functional Porous Materials, School of Materials Science and Engineering, Zhejiang Sci-Tech University, Hangzhou 310018, China. E-mail: jkgao@zstu.edu.cn
[b] College of Materials Science and Engineering, China Jiliang University, Hangzhou 310018, China
[c] State Key Laboratory of Silicon Materials, Cyrus Tang Center for Sensor Materials and Applications, School of Materials Science & Engineering, Zhejiang University, Hangzhou 310027, China. E-mail: gdqian@zju.edu.cn
[d] School of Materials Science & Engineering, Nanyang Technological University, Singapore 639798, Singapore. Email: qczhang@ntu.edu.sg
[e] Department of Materials Science and Engineering, City University of Hong Kong, Kowloon, Hong Kong SAR, China. Email: qiczhang@cityu.edu.hk

†Electronic Supplementary Information (ESI) available: Experimental section, Fig. S1–S16, Table S1-S2 are provided in the supporting information. See DOI: 10.1039/x0xx00000x

View Article Online
DOI: 10.1039/D0TA05864A

morphology control of MOFs-derived electrocatalysts is the key for the systematic study of FeNi-based electrocatalysts. We discovered that optimal morphology could not only largely improve the number of active sites, but also accurately tune the electronic structure, thus enhancing the intrinsic activity of the electrocatalysts. The optimized FeNi NSs exhibited a small overpotential of 246 mV at 10 mA cm^{-2} and an ultra-low Tafel slope of 31.2 mV dec^{-1} for OER.

2. Results and Discussion

The diverse morphologies of FeNi MOF precursors were achieved by facilely tuning the concentration of reactants with/out the addition of PVP at room temperature. Then, the possible remaining PVP in product has been carefully washed away as illustrated in the Fourier transform infrared (FT-IR) spectra as shown in Fig. S1†. Note that if there still exists a small amount of residual PVP, they will decompose at high temperature during pyrolysis (Fig. S2†). The schematic illustration of the morphology modulation strategy of FeNi MOFs-derived electrocatalysts is shown in Scheme 1. The detailed synthesis methods were provided in supporting information. We firstly prepared bimetallic MOFs with totally different micromorphology but same crystal structure. As shown in Fig. 1a, metal ions are linked to pyrazine ligands and -CN. The X-ray diffraction (XRD) patterns of the pristine Hofmann MOFs exhibit clear diffraction peaks and the peaks of four MOFs could be well consistent with the simulated results, which also indicates that crystal structures of four MOFs are same to each other (Fig. S3†). The XRD patterns of FeNi NSs, FeNi NFs, FeNi NTs and FeNi AGs exhibit same diffraction peaks (Fig. 1b). The peaks located at 26.4° can be assigned to the (002) plane of graphitic carbon[38], while the peaks appearing at 43.7° and 50.9° can be indexed into the (111) and (200) planes of $FeNi_3$ (JCPDS no. 65-3244).

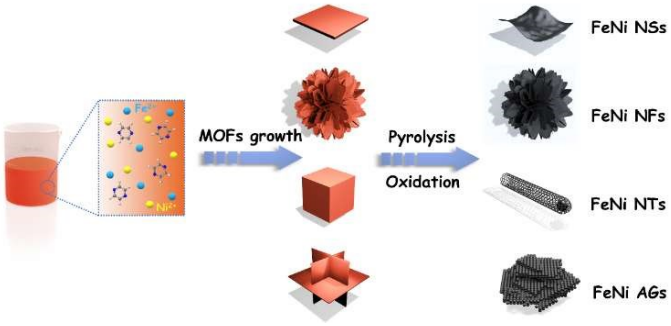

Scheme 1 The schematic illustration of FeNi Hofmann MOFs-derived electrocatalysts with different morphologies for the OER.

As confirmed by scanning electron microscopy (SEM) images, nanosheet MOFs with a side length of ca. 600 nm (Fig. 1c) were formed in a low-concentration reaction system. The morphology of the nanosheet MOFs was further characterized via atomic force microscope (AFM) and the thickness of the nanosheet was 61 nm (Fig. S4†). After pyrolysis and partial oxidation, the original smooth surface of the nanosheets became rough and crimp, while the size remained unchanged (denoted as FeNi NSs, Fig. 1g). Unique nanoflower structure was formed in a low-concentration reaction system containing the surfactant PVP. The nanoflower with a diameter of ca. 1.2 μm and a thickness of 60-80 nm was constructed by dozens of nanosheets to form 2D/3D multiscale structure (Fig. 1d). After high temperature treatment, the surface of the nanoflower became porous and crimp, however, the morphology of the nanoflower remained as same as the original one (denoted as FeNi NFs, Fig. 1h). The nanoparticles of MOFs with the size of 50-60 nm were obtained in high concentration reaction system (Fig. 1e). Interestingly, the high-temperature treatment could transform nanoparticles into bamboo-like nanotubes with a diameter of ca. 100 nm (denoted as FeNi NTs, Fig. 1i), which may be due to the nanoparticles' aggregation and catalytic effect during high temperature pyrolysis. In contrast, with the existence of PVP in a high concentration system, decussate fine nanosheet MOFs were fabricated (Fig. 1f). The aggravations were formed after pyrolysis of these decussate fine nanosheet MOFs (denoted as FeNi AGs, Fig. 1j).

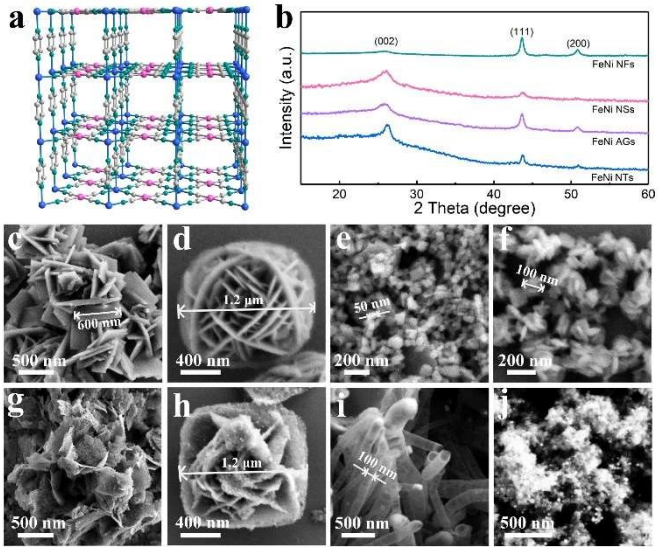

Fig. 1 (a) The crystal structure of [Fe]pyrazine[$Ni(CN)_4$] MOFs, Fe blue, Ni pink, C gray, N green. Solvent molecules and H are omitted for clarity. (b) The XRD patterns of the as-prepared catalysts. (c-f) The SEM images of the as-synthesized MOF precursors in different reaction systems. (g-j) The SEM images of FeNi NSs, FeNi NFs, FeNi NTs and FeNi AGs.

The transmission electron microscope (TEM) image of nanosheet MOFs further confirms its regular sheet structure as shown in Fig. S5†. The TEM image of FeNi NSs (Fig. 2a, Fig. S6†) indicates that metal nanoparticles (ca. 20 nm) are encapsulated in ultrafine carbon layers to form core@shell morphology, where the carbon matrix can serve as buffer to protect the composite from the structural damage during the electrocatalysis. Moreover, the high resolution-transmission electron microscope (HR-TEM) image of FeNi NSs is shown in Fig.

View Article Online
DOI: 10.1039/D0TA05866A

S7†, the lattice fringes with a spacing of 0.21 nm can be indexed into (111) plane of $FeNi_3$, which corresponds with the XRD patterns. The TEM images of FeNi NFs and FeNi AGs are similar to that of FeNi NSs, while FeNi NTs exhibited bamboo-shape nanotubes (ca. 100 nm) with abundant rumpled ridges in the middle of nanotubes. Energy dispersive spectrometer (EDS) mapping demonstrates the even distribution of Fe species, Ni species, and N species over the C matrix.

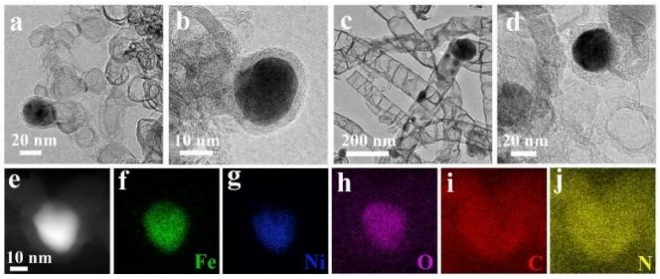

Fig. 2 (a-d) TEM images of FeNi NSs, FeNi NFs, FeNi NTs, and FeNi AGs. (e-j) The EDS mapping of Fe, Ni, O, C, and N.

Raman spectra displayed two peaks located at 1350 cm^{-1} and 1580 cm^{-1} as shown in Fig. S8†, representing D (sp^3 hybrid carbon) and G (sp^2 hybrid carbon) band, respectively. The intensity ratio of I_G/I_D can be used to measure the degree of graphitization, where a higher I_G/I_D ratio has a great contributes to higher conductivity. The ratio values of I_G/I_D increased as follows: FeNi AGs (1.04) < FeNi NFs (1.19) < FeNi NTs (1.23) < FeNi NSs (1.24), which demonstrated that FeNi NSs possessed better conductivity and electronic transmission efficiency. N_2 adsorption/desorption method was conducted to characterize the specific surface area of the as-prepared electrocatalysts (Fig. S9†). All four samples displayed type IV isotherms together with hysteresis loops at 0.4-1.0, and the specific surface area values of FeNi NSs, FeNi NFs, FeNi NTs and FeNi AGs are 226.9, 216.1, 225.7 and 227.0 $m^2\ g^{-1}$, respectively. Barrett-Joyner-Halenda (BJH) analysis revealed the pore size distribution of the as-prepared four samples (Fig. S10†). All the curves display one peak at ca. 4 nm, confirming the presence of plentiful mesopores. A rich mesoporous structure with a large surface area will facilitate the exposure of internal active sites to promote electrocatalytic activity.[37]

X-ray photoelectron spectroscopy (XPS) was employed to investigate the chemical state and composition of four electrocatalysts in Fig. 3 and Fig. S11†. Fig. 3a shows two main peaks at 710.9 eV and 724.6 eV, corresponding to Fe $2p_{3/2}$ and Fe $2p_{1/2}$ for FeNi NSs respectively. The fitted peaks located at 710.4 eV and 724.0 eV correspond to Fe^{2+} and the peaks at 711.8 eV and 725.4 eV can be assigned to Fe^{3+}. Compared to FeNi NSs, the Fe $2p_{3/2}$ and Fe $2p_{1/2}$ peaks of FeNi NFs, FeNi NTs and FeNi AGs shift to lower band successively. Furthermore, in the Ni XPS spectra (Fig. 3b), the two main peaks centered at 854.4 eV and 872.3 eV can be specified to Ni $2p_{3/2}$ and Ni $2p_{1/2}$, together with two satellite peaks situated at 860.2 eV and 878.9 eV. Interestingly, it can be clearly observed that two main peaks shifted to higher binding energy in the order of FeNi NFs, FeNi NTs and FeNi AGs compared to FeNi NSs, indicating that morphology regulation could realize the transfer of electrons from nickel ions to iron ions.[38] The synergistic effects between Fe and Ni are optimized via electronic modulation, which may be the main reason for the improvement of OER. The schematic illustration of enhancing OER performance via morphology regulation is shown in Fig. S12†. Significantly, the deconvolution of O 1s spectra of FeNi electrocatalysts yielded three characteristic peaks centered at about 530.2 eV, 531.5 eV and 532.7 eV respectively, which could be attributed to metal-oxygen bonds (O1), defective oxygen sites (O2) and hydroxyl groups (O3) as exhibited in Fig. 3c.[39,40] FeNi NSs owned a relatively higher O2 proportion (25.8%) compared to FeNi NFs (23.3%), FeNi NTs (17.8%) and FeNi AGs (12.9%). This result indicates that morphologies and structures engineering can induce abundant oxygen vacancies of defects, which can optimize the adsorption energy of the electrocatalysts for OER intermediates thereby promoting electrocatalytic properties.[41,42] N 1s spectra were shown in Fig. S13† and Fig. 3d. The N 1s spectra were fitted into five peaks for FeNi NSs, namely pyridinic N, Fe(Ni)-N_x, pyrrolic N, graphitic N and Oxidized N.[43] Among these species, Fe(Ni)-N_x is commonly deemed as electrocatalytic active sites and pyridinic N may relate to highly catalytic performance.[21,44] Moreover, detailed percentages of N species were exhibited in Fig. 3d and the density of pyridinic N was higher than that of FeNi NFs, FeNi NTs and FeNi AGs. The quantitative analyses of element content calculated via XPS is shown in Table S1†. The N content in four electrocatalysts is basically similar.

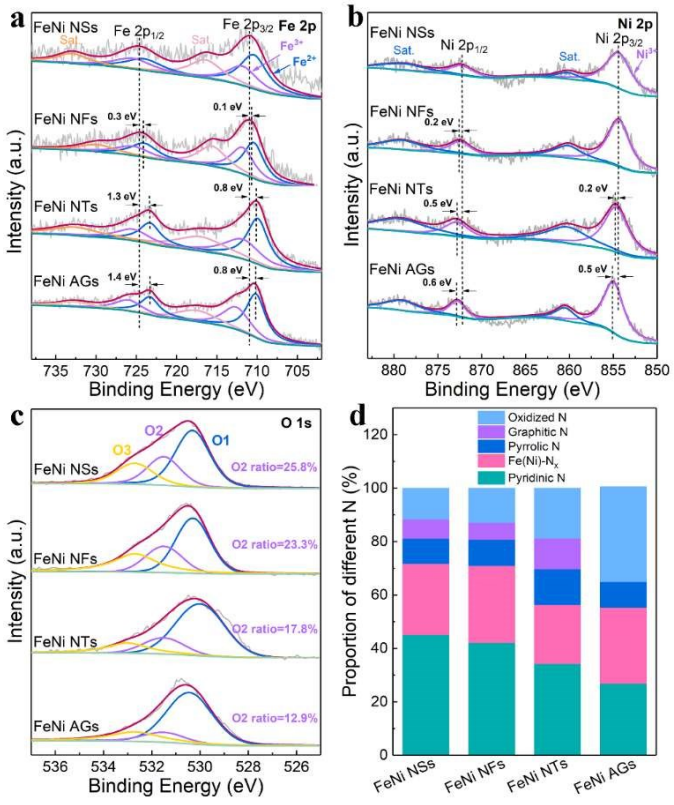

Fig. 3 The XPS spectra of (a) Fe 2p, (b) Ni 2p, and (c) O 1s. (d) N 1s result for FeNi NSs, FeNi NFs, FeNi NTs and FeNi AGs.

It can be assumed that optimized morphologies and porous structure can afford abundant exposed edge sites. More importantly, the optimized electronic structure will contribute to the synergistic effects from FeNi bimetals and N-doped carbon matrix, thereby enhancing catalytic properties in the meantime. OER activities were characterized using linear sweep voltammetry (LSV) curves in a typical three-electrode system containing 1 M KOH solution. The loading mass on the working electrode (Ni foam) was 0.8 mg cm^{-2}. Fig. 4a-b showed that the overpotentials for FeNi NSs, FeNi NFs, FeNi NTs, FeNi AGs and commercial RuO_2 at 10 mA cm^{-2} are 248 mV, 258 mV, 284 mV, 332 mV and 286 mV, respectively. In particular, the FeNi NSs displayed the best OER performance, which is 38 mV better than that of commercial RuO_2. Moreover, the current density at 1.55 V for FeNi NSs is 41.5 mA cm^{-2}, which is 7.5 mA cm^{-2}, 17.9 mA cm^{-2}, 34.3 mA cm^{-2} and 26.9 mA cm^{-2} better than those of FeNi NFs, FeNi NTs, FeNi AGs and commercial RuO_2, respectively. As for practical application potential, overpotentials at high current density are very important. FeNi NSs exhibit 334 mV@50 mA cm^{-1} and 414 mV@100 mA cm^{-1}, which are super to FeNi NFs (353 mV@50 mA cm^{-1}, 446 mV@100 mA cm^{-1}), FeNi NTs (374 mV@50 mA cm^{-1}, 462 mV@100 mA cm^{-1}), FeNi AGs (430 mV@50 mA cm^{-1}, 524 mV@100 mA cm^{-1}) and commercial RuO_2 (516 mV@50 mA cm^{-1}). Moreover, onset potentials for FeNi NSs, FeNi NFs, FeNi NTs and FeNi AGs are 1.47 V, 1.48 V, 1.52 V and 1.53 V respectively, which indicates that FeNi NSs has the best catalytic kinetics. The OER kinetics of electrocatalysts with different morphologies were further calculated by the Tafel slope as shown in Fig. 4c. The FeNi NSs exhibits smallest Tafel slope of 31.2 mV dec^{-1}, which is lower than most of the reported OER catalysts. The interfacial electron/proton transfer activity of the electrocatalysts was conducted by electrochemical impedance spectroscopy (EIS) as shown in Fig. S14†. The R_{ct} of FeNi NSs is about 18 Ω, which is obviously much smaller than those of FeNi NFs, FeNi NTs and FeNi AGs. The electrochemical active surface area (ECSA) was calculated via double-layer capacitance (C_{dl}) values as shown in Fig. S15†. The C_{dl} for FeNi NSs, FeNi NFs, FeNi NTs and FeNi AGs is calculated to be 25.2, 17.5, 11.9 and 10.5 mF cm^{-2}. It is obvious that FeNi NSs have more electroactive sites than other electrocatalysts, which leads to its superior catalytic performance. The results further indicate that morphology control can accurately control the electrochemically active sites of catalysts. The durability of FeNi NSs was also measured and compared to commercial RuO_2 as shown in Fig. 4d, and FeNi NSs could work steadily for at least 24 hours, while RuO_2 increases obviously within 8 hours. As for cyclic stability, the LSV curve of FeNi NSs only changes slightly after 1000 CVs while the two curves for RuO_2 do not coincide at all, demonstrating the eminent catalytic stability of the obtained catalyst. Fig. S16† shows the SEM image of FeNi NSs after OER and the electrocatalyst remains nanosheet morphology, indicating the structure stability of FeNi NSs. Meanwhile, FeNi NSs demonstrates top-level OER catalytic properties among recent reported MOFs-derived transition metals based electrocatalysts (Fig. 4e; Table S2†).

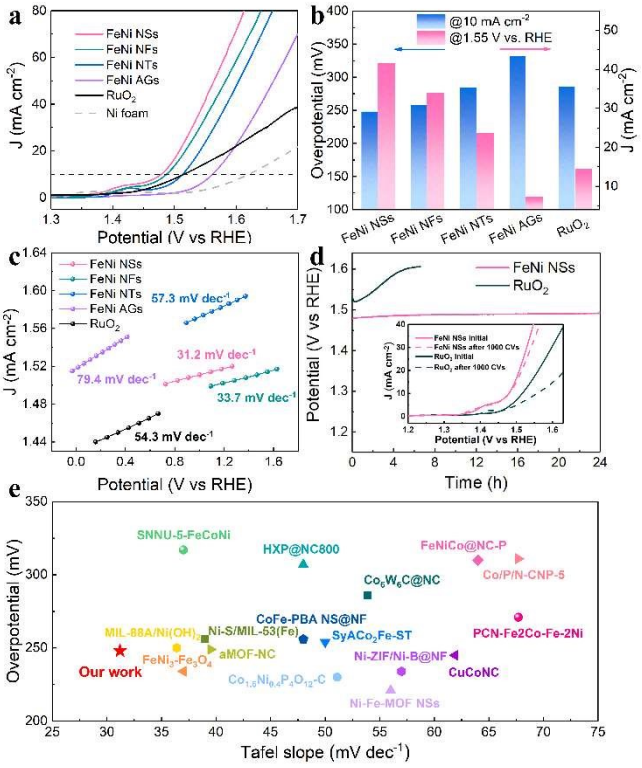

Fig. 4 (a) LSV curves of FeNi NSs, FeNi NFs, FeNi NTs, FeNi AGs and commercial RuO_2. (b) Overpotential at 10 mA cm^{-2} and the current density at 1.55 V vs. RHE of FeNi NSs, FeNi NFs, FeNi NTs, FeNi AGs and commercial RuO_2. (c) Tafel slope plots of different electrocatalysts. (d) The Chronopotentiometric curves of FeNi NSs and RuO_2 at 10 mA cm^{-2}. Inset: LSV curves before and after 1000 cycles for FeNi NSs and RuO_2. (e) Comparison of the overpotentials and Tafel slopes of our catalyst to other recently reported MOFs-derived OER electrocatalysts.

3. Conclusions

In summary, the morphology of electrocatalysts are rationally modified through facilely tuning the synthetic condition of the precursor MOFs. The precise modulation of morphology created electron transfer from nickel ions and iron ions, leading to well-tuned electronic structural properties. Moreover, the optimized FeNi NSs possesses enhanced conductivity, abundant oxygen vacancies, N-related active sites and electrocatalytic active sites. FeNi NSs exhibited superior OER properties with a small overpotential of 248 mV at the current density of 10 mA cm^{-2}, an ultra-low Tafel slope of 31.2 mV dec^{-1}, outperforming FeNi NFs, FeNi NTs, FeNi AGs and commercial RuO_2. Our work may provide a new insight into the systematic regulation of catalysts morphology for performance enhancement in electrocatalysis and photocatalysis.

Conflicts of interest

The authors declare no conflict of interest.

Acknowledgements

This work was supported by Natural Science Foundation of Zhejiang Province (No. LY19E020007). J. G. acknowledges the financial support from the Fundamental Research Funds of Zhejiang Sci-Tech University (2019Q007). Q.Z. acknowledges financial support from AcRF Tier 1 (RG 111/17, RG 2/17, RG 114/16, RG 8/16) and Tier 2 (MOE 2017-T2-1-021 and MOE 2018-T2-1-070), Singapore. QZ also thanks the support from State Key Laboratory of Supramolecular Structure and Materials, Jilin University (sklssm2020041).

References

1 Z. W. Seh, J. Kibsgaard, C. F. Dickens, I. Chorkendorff, J. K. Nørskov and T. F. Jaramillo, *Science*, 2017, **355**, eaad4998.
2 C. Hu, L. Zhang and J. Gong, *Energy Environ. Sci.*, 2019, **12**, 2620–2645.
3 H. Yin and Z. Tang, *Chem. Soc. Rev.*, 2016, **45**, 4873–4891.
4 X. Zhang, X. Cheng and Q. Zhang, *J. Energy. Chem*, 2016, **25**, 967–984.
5 J. Zhang, Q. Zhang and X. Feng, *Adv. Mater.*, 2019, **31**, 1808167.
6 B. Xiong, L. Chen and J. Shi, *ACS Catal.*, 2018, **8**, 3688–3707.
7 P.-Q. Liao, J.-Q. Shen and J.-P. Zhang, *Coord. Chem. Rev.*, 2018, **373**, 22–48.
8 Y. Liu, X. Li, Q. Zhang, W. Li, Y. Xie, H. Liu, L. Shang, Z. Liu, Z. Chen and L. Gu, *Angew. Chem. Int. Ed.*, 2020, **59**, 1718–1726.
9 B. Zhu, D. Xia and R. Zou, *Coord. Chem. Rev.*, 2018, **376**, 430–448.
10 Y. Lin, H. Wan, D. Wu, G. Chen, N. Zhang, X. Liu, J. Li, Y. Cao, G. Qiu and R. Ma, *J. Am. Chem. Soc.*, 2020, **142**, 7317–7321.
11 H. Wang, Q.-L. Zhu, R. Zou and Q. Xu, *Chem*, 2017, **2**, 52–80.
12 (a) X.-L. Wang, L.-Z. Dong, M. Qiao, Y.-J. Tang, J. Liu, Y. Li, S.-L. Li, J.-X. Su and Y.-Q. Lan, *Angew. Chem. Int. Ed.*, 2018, **57**, 9660–9664; (b) D.-D. Huang, S. Li, Y.-P. Wu, J.-H. Wei, J.-W. Yi, H.-M. Ma, Q. Zhang, Y.-L. Liu and D. Li, *Chem. Commun.*, 2019, **55**, 4570-4573; (c) S. Guo, X. Chen, F. Hu, Q. Zhang and L. Liu, *ACS Appl. Mater. Interfaces*, 2015, **7**, 20164-20169; (d) G. Luo, H. Zhang, Y. Tao, Q. Wu, D. Tian and Q. Zhang, *Inorg. Chem Front.*, 2019, **6**, 343 – 354.
13 Y. Xiao, T. Hu, X. Zhao, F. X. Hu, H. B. Yang, C. M. Li, Nano Energy 2020, **75**, 104949.
14 J. Song, C. Wei, Z.-F. Huang, C. Liu, L. Zeng, X. Wang and Z. J. Xu, *Chem. Soc. Rev.*, 2020, **49**, 2196–2214.
15 Z.-P. Wu, X. F. Lu, S.-Q. Zang and X. W. Lou, *Adv. Funct. Mater.*, 2020, **30**, 1910274.
16 Y.-J. Tang, H.-J. Zhu, L.-Z. Dong, A.-M. Zhang, S.-L. Li, J. Liu and Y.-Q. Lan, *Appl. Catal. B-Environ.*, 2019, **245**, 528–535.
17 M. Zhao, H. Li, W. Yuan, C. M. Li, ACS Appl. Energy Mater. 2020, **3**, 3966.
18 J. S. Kim, B. Kim, H. Kim and K. Kang, *Adv. Energy Mater.*, 2018, **8**, 1702774.
19 Y. Zhu, W. Sun, W. Chen, T. Cao, Y. Xiong, J. Luo, J. Dong, L. Zheng, J. Zhang, X. Wang, C. Chen, Q. Peng, D. Wang and Y. Li, *Adv. Funct. Mater.*, 2018, **28**, 1802167.
20 Z.-Y. Wu, W.-B. Ji, B.-C. Hu, H.-W. Liang, X.-X. Xu, Z.-L. Yu, B.-Y. Li and S.-H. Yu, *Nano Energy*, 2018, **51**, 286–293.
21 J. Ding, P. Wang, S. Ji, H. Wang, V. Linkov and R. Wang, *Electrochim. Acta*, 2019, **296**, 653–661.
22 J. Wang and F. Ciucci, *Small*, 2017, **13**, 1604103.
23 H. Jin, J. Wang, D. Su, Z. Wei, Z. Pang and Y. Wang, *J. Am. Chem. Soc.*, 2015, **137**, 2688–2694.
24 Y. Li, M. Lu, Y. Wu, H. Xu, J. Gao and J. Yao, *Adv. Mater. Interfaces*, 2019, **6**, 1900290.
25 Z. Zhai, C. Li, L. Zhang, H.-C. Wu, L. Zhang, N. Tang, W. Wang and J. Gong, *J. Mater. Chem. A*, 2018, **6**, 9833–9838.
26 X. Ma, W. Zhang, Y. Deng, C. Zhong, W. Hu and X. Han, *Nanoscale*, 2018, **10**, 4816–4824.
27 H. Du, W. Ai, Z. L. Zhao, Y. Chen, X. Xu, C. Zou, L. Wu, L. Su, K. Nan, T. Yu and C. M. Li, *Small*, 2018, **14**, 1801068.
28 D. Liu, J. Wan, G. Pang and Z. Tang, *Adv. Mater.*, 2019, **31**, 1803291.
29 H.-F. Wang, L. Chen, H. Pang, S. Kaskel and Q. Xu, *Chem. Soc. Rev.*, 2020, **49**, 1414–1448.
30 L. Du, L. Xing, G. Zhang and S. Sun, *Carbon*, 2020, **156**, 77–92.
31 Y. Yan, C. Li, Y. Wu, J. Gao and Q. Zhang, *J. Mater. Chem. A*, 2020, DOI: 10.1039/D0TA03749D.
32 J. Gao, X. Qian, R.-B. Lin, R. Krishna, H. Wu, W. Zhou and B. Chen, *Angew. Chem. Int. Ed.*, 2020, **59**, 4396-4400.
33 Y. Li, T. Zhao, M. Lu, Y. Wu, Y. Xie, H. Xu, J. Gao, J. Yao, G. Qian and Q. Zhang, *Small*, 2019, **15**, 1901940.
34 C. Li, H. Xu, J. Gao, W. Du, L. Shangguan, X. Zhang, R.-B. Lin, H. Wu, W. Zhou, X. Liu, J. Yao and B. Chen, *J. Mater. Chem. A*, 2019, **7**, 11928-11933.
35 J.-X. Wu, C.-T. He, G.-R. Li and J.-P. Zhang, *J. Mater. Chem. A*, 2018, **6**, 19176–19181.
36 X. Zhao, P. Pachfule, S. Li, J. R. J. Simke, J. Schmidt and A. Thomas, *Angew. Chem. Int. Ed.*, 2018, **57**, 8921–8926.
37 S. Chen, S. Chen, B. Zhang and J. Zhang, *ACS Appl. Mater. Interfaces*, 2019, **11**, 16720–16728.
38 J.-G. Li, H. Sun, L. Lv, Z. Li, X. Ao, C. Xu, Y. Li and C. Wang, *ACS Appl. Mater. Interfaces*, 2019, **11**, 8106–8114.
39 Z. Ye, C. Qin, G. Ma, X. Peng, T. Li, D. Li and Z. Jin, *ACS Appl. Mater. Interfaces*, 2018, **10**, 39809–39818.
40 S. Peng, F. Gong, L. Li, D. Yu, D. Ji, T. Zhang, Z. Hu, Z. Zhang, S. Chou, Y. Du and S. Ramakrishna, *J. Am. Chem. Soc.*, 2018, **140**, 13644–13653.
41 Q. Hu, X. Huang, Z. Wang, G. Li, Z. Han, H. Yang, X. Ren, Q. Zhang, J. Liu and C. He, *J. Mater. Chem. A*, 2020, **8**, 2140–2146.
42 X. Li, S. You, J. Du, Y. Dai, H. Chen, Z. Cai, N. Ren and J. Zou, *J. Mater. Chem. A*, 2019, **7**, 25853–25864.
43 S. Ibraheem, S. Chen, J. Li, W. Li, X. Gao, Q. Wang and Z. Wei, *ACS Appl. Mater. Interfaces*, 2019, **11**, 699–705.
44 K. Wu, X. Chen, S. Liu, Y. Pan, W.-C. Cheong, W. Zhu, X. Cao, R. Shen, W. Chen, J. Luo, W. Yan, L. Zheng, Z. Chen, D. Wang, Q. Peng, C. Chen and Y. Li, *Nano Res.*, 2018, **11**, 6260–6269.

View Article Online
DOI: 10.1039/D0TA05866A

Table of Contents Only

A series of morphology-regulated oxygen-evolution electrocatalysts including nanosheets, nanoflowers, nanotubes and aggregations derived from Hofmann-type metal-organic frameworks have been developed and demonstrated as efficient oxygen evolution electrocatalysis.